Materials Science & Engineering A 952 (2026) 149614

Contents lists available at ScienceDirect

Materials Science & Engineering A

journal homepage: www.elsevier.com/locate/msea

Quenching & partitioning vs. direct tempering in powder bed fusion – Laser beam AISI 420: Impact on microstructural features and mechanical behavior

M. Belfi [a], G. Lupi [a], P. Martin [b], M. Santofimia [c], A. Gruttadauria [a], R. Casati [a,**], S. Barella [a,*]

[a] Department of Mechanical Engineering, Politecnico di Milano, 20156, Milano, Italy
[b] Departamento de Ingeniería de Minas, Metalurgia y Materiales, Universidad Técnica Federico Santa María, 2390123, Valparaíso, Chile
[c] Department of Materials Science and Engineering, TU DelftCD Delft, 2628, the Netherlands

ARTICLE INFO

Keywords:
Additive manufacturing
Laser powder bed fusion
Tempering
Quenching and partitioning
Retained austenite

ABSTRACT

Powder Bed Fusion – Laser Beam (PBF-LB) processing of AISI 420 martensitic stainless steel enabled the production of fully dense components. The as-built condition exhibited a fine martensitic matrix with a high fraction of retained austenite (16 %), leading to high tensile strength (1555 MPa) but limited ductility (7 %). To enhance mechanical performance, different heat-treatment strategies were investigated. Direct tempering significantly improved ductility to 15 % while maintaining high strength (UTS of 1589 MPa), primarily attributed to the reduction of residual stress and tempering of martensite. Alternatively, quenching and partitioning treatments allowed further tuning of the microstructure, leading to a homogeneous distribution of stable retained austenite in a martensitic matrix. The most effective condition partitioned at 450 °C for 10 min, led to 11 % retained austenite, achieving a UTS of 1358 MPa and 18 % elongation. In contrast, applying a partitioning temperature of 250 °C for the same time resulted in a higher UTS (1683 MPa) but lower ductility (5 %) due to reduced austenite stability and martensite tempering. The work-hardening behavior of the material was modified by the processing technique and the consequent features of the introduced microstructure. Both direct tempering and quenching and partitioning demonstrated promising strength-ductility combinations, showing that tailored heat treatments can optimize the mechanical response of PBF-LB AISI 420 steel for high strength applications.

1. Introduction

In recent years, Advanced High-Strength Steels (AHSS) have achieved unprecedent sets of tensile properties [1]. In this scenario, the high tensile properties and ductility of the third generation of AHSS have allowed reducing the resistant sections of components while maintaining high safety and impact toughness in automotive applications [2]. The third generation of AHSS is characterized by tailored microstructures, usually multiphase, obtained through specific chemical compositions and innovative heat treatments. One of the most promising of these heat treatments, the Quenching and Partitioning (QP) heat treatment, aims to stabilize a significant fraction of retained austenite (RA) into a martensitic microstructure, leading to high tensile properties coupled with improved ductility [3]. The treatment consists of a full (or seldom partial) austenitization, followed by an incomplete quenching below the martensite start temperature (M_s). At this step the microstructure is composed of martensite and a fraction of untransformed austenite. An isothermal treatment called partitioning is then performed. During this stage, carbon diffuses from the supersaturated martensite into austenite, stabilizing the austenite at room temperature [4]. Finally, a second quench to room temperature is performed in which a fraction of the austenite may transform into fresh martensite (FM) if its stabilization was not completed during partitioning.

FM is detrimental for the mechanical properties, reducing especially the ductility, thus it should be avoided through a correct design of the treatment [5]. The fraction of austenite at the quenching step, and therefore the selection of the initial quenching temperature, is crucial, as an excessive fraction of austenite resulting from the first quenching is

* Corresponding author.
** Corresponding author.
E-mail addresses: riccardo.casati@polimi.it (R. Casati), silvia.barella@polimi.it (S. Barella).

https://doi.org/10.1016/j.msea.2025.149614
Received 5 September 2025; Received in revised form 3 December 2025; Accepted 11 December 2025
Available online 17 December 2025

typically responsible for the formation of FM [6]. Quenching temperatures introducing an initial fraction of around 15–20 % of austenite have been reported to be optimal for achieving the targeted final microstructure [7,8]. RA increases the ductility of the material and may transform into martensite through a strain-induced transformation (TRIP effect) when subjected to an external load, contributing to the high tensile properties [9]. Besides, this transformation delays the onset of necking, increasing the ductility and especially uniform elongation (UE) compared to the fully martensitic condition [10,11]. Not only the fraction of RA, but its mechanical stability, morphology, size and distribution influence the final properties of the material [12,13].

The choice of steel with suitable chemical composition is of major importance to control the microstructure development during the QP process and the final mechanical properties. As the process is based on carbon diffusion, the precipitation of carbides that trap carbon and prevent it from stabilizing the austenite must be limited. This is done typically by the addition of Si (and more rarely, Al) in amounts greater than 1 wt% [8]. Although the precipitation of transition carbides is not completely suppressed by Si, this element delays the precipitation of cementite and ensures a more effective diffusion process [14]. Moreover, it has also been observed that Si can directly promote the stabilization of austenite [15]. Mn is introduced to further facilitate austenite stabilization and to guarantee an improved hardenability of the material [16]. Elevated Si and Mn contents are however difficult to handle in the steel production process, and at present, special steels for high-strength applications in production routinely have lower Si concentrations. Consequently, some effort has been set on applying the QP treatment on commercially available steels whose chemical composition is not optimized for QP [17–20] for applications where a combination of high mechanical strength and ductility is of major interest.

AISI 420 is a martensitic stainless steel featuring high hardness, strength, and wear resistance, with potential for the applicability of the QP process. Mola and De Cooman [6] reported that a significant fraction of RA can be successfully stabilized in AISI 420 steel with different QP processing routes, reaching tensile strengths above 1500 MPa and ductility higher than 14 %. Barella et al. [21] applied single- and double-step QP treatments on AISI 420 obtaining 1800 MPa coupled with 10 % elongation in the first case, and 1600 MPa coupled with 20 % elongation in the latter. These two studies were performed on AISI 420 obtained by conventional production processes.

AISI 420 has repeatedly shown compatibility to laser Additive Manufacturing (AM) processes, showing excellent processability through Powder Bed Fusion – Laser Beam (PBF-LB) [22,23]. The application of AM is expanding as it allows for the creation of complex geometries and the achievement of specific performance requirements that are not possible to obtain directly by traditional methods [24–26]. In particular, the rapid cooling experienced during AM enables the formation of martensite phases in AISI 420, resulting typically in high hardness, high strength, and low ductility [27]. For example, Nath et al. reported an as-built AISI 420 exhibiting an ultimate tensile strength of 1050 MPa, yield strength of 700 MPa, and elongation of 2.5 % [28]. Such low elongation and the presence of residual stresses justifies the design of post-processing heat treatment schedules in AM-ed parts [29].

In this regard, the QP heat treatment is a promising candidate for post-processing of AM-ed components. Direct tempering (DT) of as-build AM-ed parts, which exhibit a martensitic microstructure, may also be an interesting option. Tempering on martensitic steel is normally done after quenching to relieve residual stresses and the intrinsic brittleness of the fresh martensite while improving ductility. However, since AM-manufactured low-alloy steel already exhibits martensitic microstructure, tempering can be applied directly to the sample in the as-build condition [26]. Nath et al. studied the effect of low-T tempering (315 °C for 2 h) on a PBF-LB manufactured AISI 420, which led to high ultimate tensile strength (1520 MPa), yield strength (950 MPa), and elongation (6.3 %) without appreciable change in hardness [28,36].

This work aims to explore the application of the QP and DT on a commercially available martensitic stainless steel that was not specifically designed for this treatment, and which was manufactured using PBF-LB. With this aim, AISI 420 samples were produced through PBF-LB and then subjected to QP and direct tempering. A controlled microstructure and high mechanical properties are targeted. The effectiveness of the treatments was critically discussed both regarding development of microstructural features and tensile properties. Lastly, a comparison between the QP and specifically designed comparative QT samples is performed.

2. Materials and methods

AISI 420 powder with particle size range of 15–45 μm was procured from Mimete s.r.l. The nominal composition of the alloy powder is shown in Table 1, while Fig. 1a shows SEM image of the AISI420 powder feedstock.

A Renishaw AM250 equipped with Reduced Built Volume (RBV) module was used to print cubic samples (8x8x8 mm^3) for density and microstructural analyses. The optimal combination of parameters is reported in Table 2. The scan strategy adopted involved stripes rotated by 67° after each layer (Fig. 1b), with only hatch scanning performed and without any contour creation. Specimens for dilatometric analysis and tensile tests (dimensions are reported below) were printed with the same parameters. Microstructural analysis of the material was performed by a light optical microscope (LOM) and JSM-IT 100 Scanning Electron Microscope (SEM). Electro Backscatter Diffraction (EBSD) analyses of the AB and DT sample were performed with Zeiss Sigma 500VP field-emission scanning electron microscope (FE-SEM) and Carl Zeiss EVO 50 field emission gun scanning electron microscope (SEM) employing a 0.1 μm step size. Samples for metallography were prepared following common grinding and polishing procedures. Microstructures were analyzed on a cross-section of the dilatometry samples. This section was taken perpendicular to the building direction and was positioned at half the sample height. Chemical etching was performed using Acqua Regia (3:1 mixture of HCl and HNO_3 + glycerol) to reveal the microstructural features. The density of samples was determined by analysis of LOM images of three cross sections of unetched samples. ImageJ software was used to obtain the fraction of pores on the total inspected area.

Bähr 805A/D dilatometer was used to heat treat the material specimens and to identify phase transformations. Cylindrical samples of Ø4 mm and 10 mm of height were tested. The specimens were heated up by induction coil under vacuum conditions (10^{-4} mbar) and cooled down employing He gas flow. An S-type thermocouple was spotwelded on the surface of each specimen to monitor the temperature during the test.

Different heat treatments were employed, whose parameters are summarized in Table 3, where T_q stands for quenching temperature, t_q for quenching time, T_p for partitioning temperature, T_T for tempering temperature, t_p for partitioning time, and t_T for tempering time. A schematic of the heat treatments is depicted in Fig. 2.

For the design of QP treatments, austenitization temperature and time were selected to guarantee full austenitization and carbide solubilization, based on previous studies on AISI 420 [21,30]. The heating rate was set as 10 °C/s, whereas a cooling rate of 25 °C/s both for the first and second quenching phase to hinder phase transformation during cooling was utilized. Two partitioning temperatures (T_p) were selected: 250 °C and 450 °C. The former is performed at temperatures employed elsewhere for single-step treatments [19–22,31]. On the other hand, a T_p of 450 °C is a conventional partitioning temperature investigated previously also on bulk AISI 420 with remarkable results both in terms of

Table 1
Nominal chemical composition of the AISI 420 powder (wt.%).

	C	Cr	Si	Mn	S	P	Fe
AISI 420 (powder)	0.25	13.5	0.33	0.4	0.004	0.011	Balance

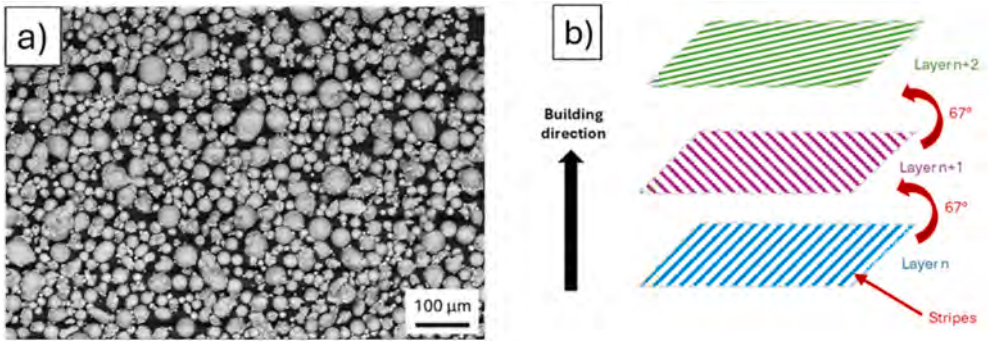

Fig. 1. a) SEM image of the AISI420 powder feedstock and b) schematic of the scan pattern.

Table 2
Process parameters used to print the samples.

Laser power	200 W
Time of exposure	110 µs
Point distance	75 µm
Hatch distance	115 µm
Layer thickness	30 µm

Table 3
Heat treatment parameters.

Specimen	Austenitization	T_q [°C]	t_q [min]	T_p/T_T [°C]	t_p/t_T [min]
Q	1100 °C, 5 min	25	–	–	–
250–10	1100 °C, 5 min	99	1	250	10
250–30	1100 °C, 5 min	99	1	250	30
450–5	1100 °C, 5 min	99	1	450	5
450–10	1100 °C, 5 min	99	1	450	10
DT	–	–	–	450	10
450–10-QT	1100 °C, 5 min	25	–	450	10

the fraction of RA and tensile properties [6,30]. Comparative QT sample 450-10-QT refers to a sample quenched down to room temperature and then tempered at 450 °C for 10 min, which aims to obtain the same martensite tempering degree of the 450-10 QP sample. An AB sample was directly tempered at 450 °C for 10 min, and it is named DT.

Microstructures were analyzed by X-ray diffraction (XRD) using a Bruker D8 Advance diffractometer with Bragg-Brentano geometry equipped with a graphite monochromator and Vantec position-sensitive detector and a Co-Kα tube. The selected range was 30–130°, with a step size of 0.035°, and a counting time per step of 1 s. A V6 Divergence slit was employed, as well as a scatter screen of 8 mm. The tube voltage and current were set at 40 kV and 40 mA, respectively. No spinning was imposed. MAUD software was employed to perform the Rietveld refinement analysis [32]. This was conducted using a pseudo-Voigt function, Popa rules size-strain model, Popa LB line broadening model, and E-WIMW texture model for the profile fittings. Additionally, Lanthanum Hexaboride Powder LaB6_660c standard reference material was utilized to determine instrumental broadening and instrumental offset. Two figures of merit (σ and R_{wp}) were used as indications of adequate refinement, considering upper limit values respectively of 2 and 10 %. Carbon concentration in austenite was computed through a modified Dyson-Holmes equation [33,34] as follows:

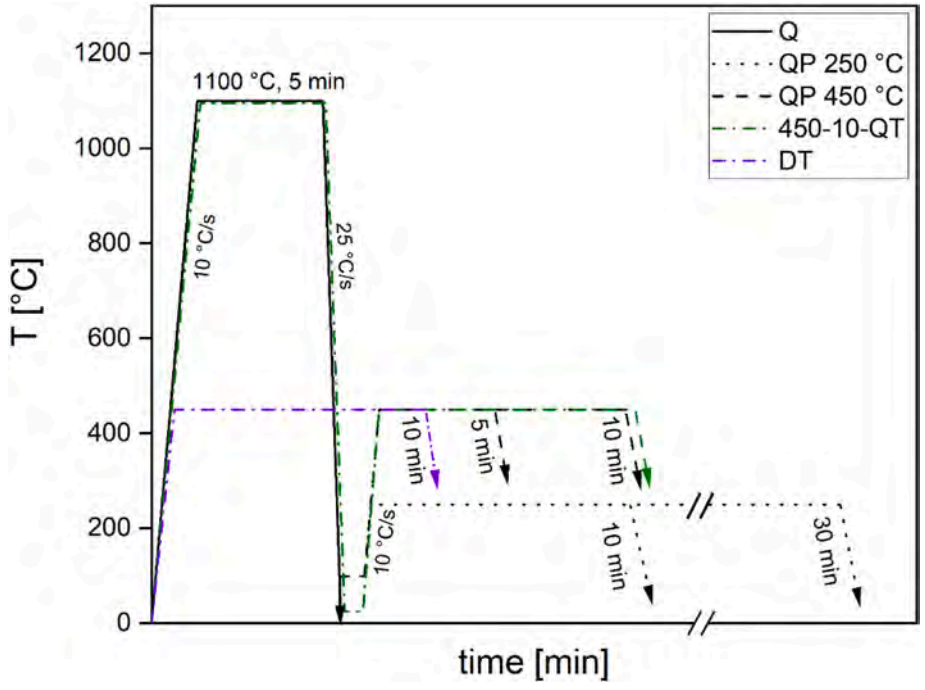

Fig. 2. Schematic of the performed heat treatments.

$$a_\gamma[\text{Å}] = 3.556 + 0.0453X_c + 0.00095X_{Mn} + 0.0056X_{Al} \quad \text{Eq. 1}$$

Where a_γ corresponds to the austenite lattice parameter, X_c to the carbon concentration, X_{Mn} to the manganese concentration, and X_{Al} to the aluminium content (all in wt.%). Microhardness tests were performed with 10 s dwell time and 300 g_f load on the different samples. 10 measurements per condition were performed. Tensile tests were carried out using a MTS100 universal testing machine equipped with a 100 kN load cell, with a crosshead speed of 2.0 mm/min. The tests were performed on flat samples machined by electrical discharge machining starting from the as-built parallelepiped-shaped plates (L 57 x W 3 x H 9 mm^3) printed orthogonally to the building direction. Tensile samples were heat treated in a muffle furnace, and isothermal treatments were performed in salt baths. The tensile sample is presented in Fig. 3.

3. Results and discussion

1. Microstructural characterization of the material in AB and DT conditions

Fig. 4a shows a representative LOM image of a section parallel to the building direction (Z) of the material in the as-built (AB) condition. The selected parameters produced nearly fully dense (99.7 ± 0.2 %) and crack-free samples, demonstrating the excellent processability of this material with PBF-LB. Although consistent carbon content increases crack susceptibility during rapid cooling, optimized printing parameters effectively mitigated this issue [22,35]. Chemical etching allowed to observe solidified melt pools generated during PBF-LB manufacturing [36]. SEM images in Fig. 4b and c show that the microstructure in the AB and DT condition, respectively, is mainly composed of austenitic cells partially transformed into fine martensitic needles due to the rapid cooling. These microstructural features have been also observed and reported in literature [22,29].

XRD measurements were performed to investigate the fraction of RA and its lattice parameter (a_γ) in the AB and DT samples. The results are presented in Table 4.

Results indicate that the thermal cycles induced by PBF-LB locally created the conditions for the stabilization of austenite at room temperature (16 ± 1 %). The DT sample showed a similar fraction of RA (15 ± 1 %), meaning that the tempering did not reduce the amount of this phase [37]. This behavior has been observed previously, as several studies have reported that martensitic steels produced by PBF-LB contain more retained austenite compared to the same grades manufactured by conventional methods [38,39]. Consistently, the austenite lattice parameters (a_γ) and consequently the austenite carbon content are increased in both samples, meaning that carbon enrichment in austenite has occurred.

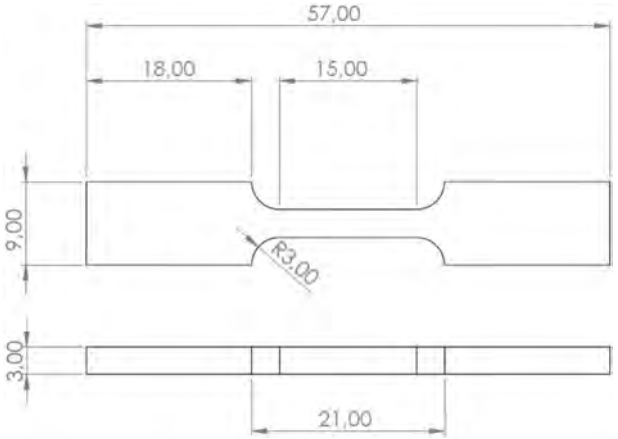

Fig. 3. Specimen for tensile testing. Indicated dimensions in mm.

EBSD analysis was employed to investigate morphology, size, and location of the RA. Results are presented in Fig. 5.

In Fig. 5a and d, the IPF images reveal a random crystallographic orientation of fine elongated grains in both cases, as observed in literature for PBF-LB samples [40–42]. In Fig. 5b and e, the phases are identified as follows: red represents the BCC (body cubic centered) phase, while yellow represents austenite (FCC). The results confirm the presence of a dual-phase microstructure featuring a considerable amount of untransformed austenite, in agreement with XRD results. Fig. 5c and f shows the distribution of austenite grains, where it is possible to observe that neighboring RA regions that share the same crystallographic orientation, suggesting they likely belong to the same parent austenite grain (PAG) [7]. These regions of common crystallographic orientation are circumscribed, providing further evidence of the fine microstructure achieved through the manufacturing process. The presence of austenite in colonies is often suboptimal for the tensile properties, as it might lead to localized variations in mechanical properties, affecting the tensile behavior of the steel [43,44].

2. Application of QP treatments

Q and QP treatments were applied in as-built specimens through dilatometry to investigate the phase evolution during the heat treatments. The dilatometric curves are reported in Fig. 6. During the heating towards austenitization, all the samples exhibited contraction events at practically the same temperatures, associated with carbide dissolution and then ferrite/martensite-to-austenite transformation. During quenching, no significant variations in the slope were observed between 1100 °C (austenitization temperature) and M_s (of approximate 200 °C, evidenced by a considerable sample expansion), indicating that phase transformations were successfully avoided in this temperature range as the selected cooling rate was higher than the critical one for an effective quenching.

Different behaviors were observed during the reheating and partitioning steps depending on the partitioning temperature, as shown in Fig. 7. Specimens reheated to 250 °C presented a practically constant slope up to the partitioning temperature, where a contraction is observed during the partitioning step. Mola et al. [6] observed a contraction during partitioning at temperatures between 200 °C and 300 °C in AISI 420, attributed to the 1st and 3rd stage of tempering, namely precipitation of transition carbides and their dissolution and cementite precipitation, which leads to an overall contraction of the material. These phenomena may be behind the slight contraction during heating at around 350 °C in the specimen partitioned at 450 °C. During the partitioning at 450 °C, a dilatation of up to 0.015 % is observed. Such expansion can be associated with carbon enrichment of the austenite. Such small changes in length exclude the occurrence of the bainitic transformation during isothermal treatment, since this type of transformation is associated with significant expansion, as observed by Kumar et al. [45] and Findley et al. [46].

Regarding the final quenching, specimens partitioned at 450 °C did not present evidence of fresh martensite formation, based on the constant slope exhibited in their dilatometry curves. This agrees with the objectives of the QP treatment, aiming to increase the stability of austenite during the partitioning step to a level in which the formation of fresh martensite is avoided. In the case of the specimens partitioned at 250 °C, a slight expansion was observed in both of their curves at practically the same temperature (around 50 °C) introducing the possibility of fresh martensite formation. Hence, this suggests that the partitioning temperature and/or time was not high enough to facilitate carbon diffusion into austenite grains. On the other hand, QP samples showed an increased slope in the second quenching phase with respect to the quenched condition. This variation can be associated with the presence of austenite during the cooling phase [6], which has a different thermal expansion coefficient than martensite [47]. The microstructure after heat treatment is composed of tempered martensite and retained

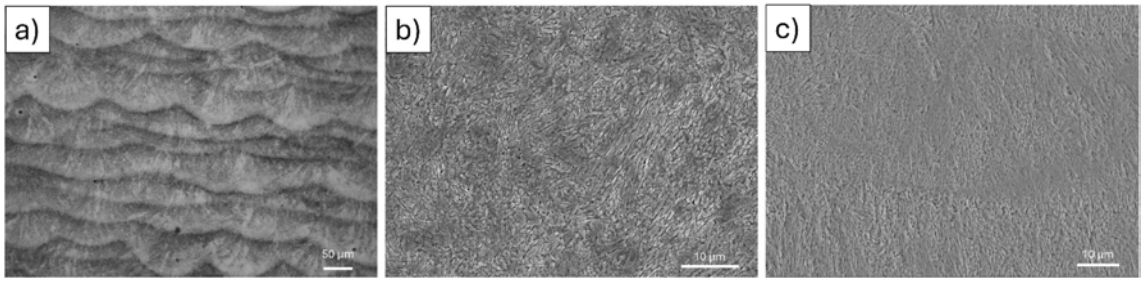

Fig. 4. Microscopy of the AB material. a) Optical microscopy of the melt pools, b) SEM picture of AB sample, c) SEM picture of the DT sample.

Table 4
Austenite quantification in AB and DT samples.

Sample	RA %	a_γ [Å]	C_γ[wt. %]
AB	16 ± 1	3.613	1.07
DT	15 ± 1	3.611	1.02

austenite in all the different QP conditions, but a minimal fraction of fresh martensite cannot be discarded in the samples partitioned at 250 °C.

Table 5 displays the measurements of RA fraction, austenite lattice parameters (a_γ) and carbon contents in austenite for the four QP samples determined. The XRD diffractograms of the QP samples in Fig. 8 showed exclusively the presence of α (BCC) and γ (FCC) peak sets. A fraction of RA between 8 and 11 % was stabilized in the QP samples. Condition 450-10 showed the highest fraction of RA at room temperature (11 %). A little fraction of untransformed austenite (1 %) was detected in the as-quenched condition. The first austenite peak (Fig. 8b), corresponding to (111) family of planes, is shifted towards lower 2θ° angles in the pattern of samples treated at 450 °C compared to those of the samples treated at 250 °C. This shift can be attributed to an increase in the carbon content in specimens partitioned at 450 °C since this causes lattice expansion, which results in the peak shifting towards lower angles [48].

As a general rule, for a specific steel composition and at constant temperature, the larger the a_γ the higher the carbon content in RA leading to improved mechanical stability [8,28]. Moreover, the samples treated at 450 °C showed higher RA fraction compared to those treated at 250 °C, which can be attributed to a difference in the thermal stability of austenite of austenite, as confirmed from the potential formation of fresh martensite during the final quench of 250 samples.

RA fractions were computed also through dilatometry in comparison with XRD results. The procedure used for quantitative phase analysis is based on the works of Mola et al. [6] and Kumar et al. [45]. A curve corresponding to 100 %-γ was extrapolated by extending the part of the curve obtained in cooling during the quenching phase (Fig. 9). The difference between the $\Delta L/L_0$ given by the extrapolated curve and the one obtained in the dilatometric curve is computed. The latter curve is not corresponding to a 100 % martensite condition because of the small remaining austenite fraction present at room temperature, as determined by XRD. By considering the RA% at room temperature, measured by XRD in the as-quenched condition, the upper limit of the lever rule (A') and the new slope of the interpolation curve were computed, corresponding to an extrapolated 100 % martensite condition.

$$\frac{\overline{A'C}}{\overline{A'B'}} = 0.01$$

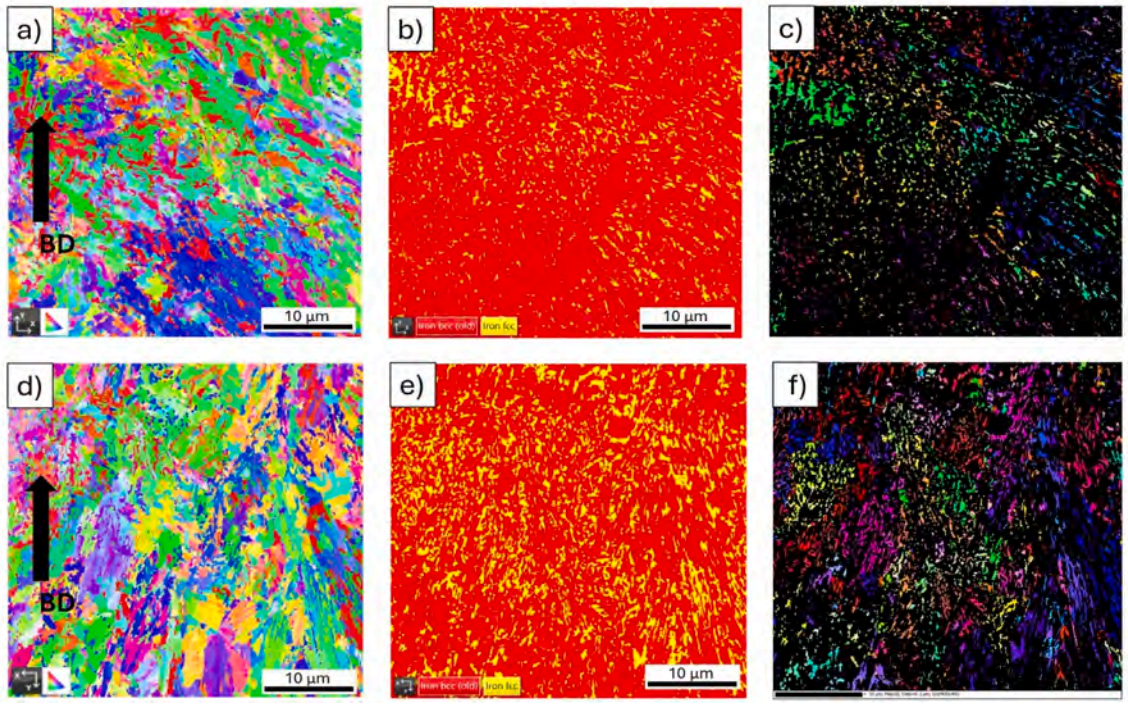

Fig. 5. EBSD analysis of the AB (a,b,c) and DT (d,e,f) samples. a),d) BCC and FCC Inverse Pole Figure (IPF), b), e) Phase map (austenite in yellow), c),f) IPF of the γ-FCC (face-cubic centered) phase subset. (For interpretation of the references to colour in this figure legend, the reader is referred to the Web version of this article.)

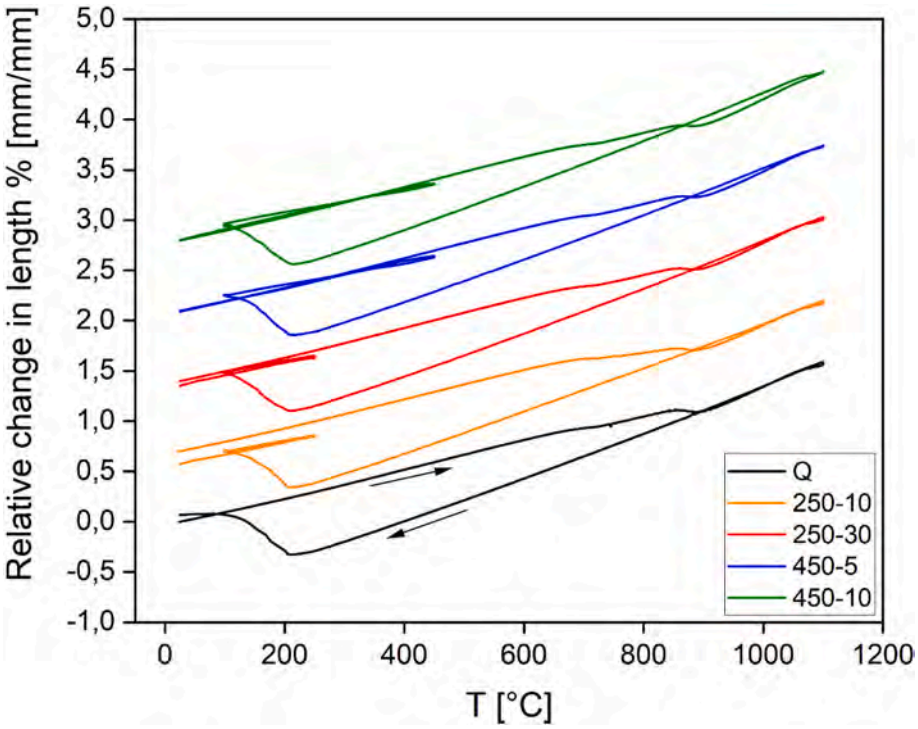

Fig. 6. Dilatometric curves for the heat-treated samples.

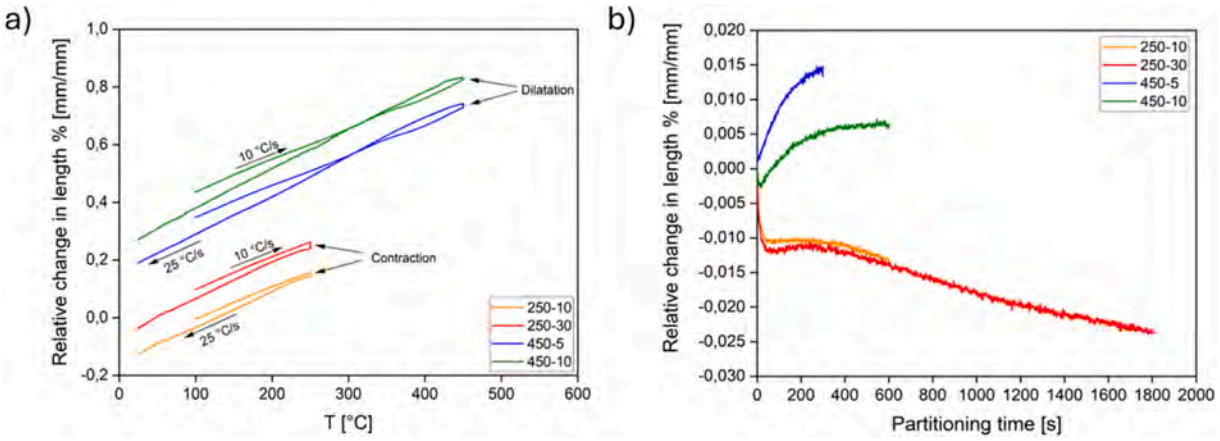

Fig. 7. Details of the dilatometry curves of QP treatments. a) Reheating, partitioning, and final quenching, b) Partitioning as a function of time.

Table 5
Results of the analysis of the XRD data.

Sample	RA %	a_γ [Å]	C_γ [wt.%]
250–10	8 ± 1	3.589	0.72
250–30	8 ± 1	3.591	0.76
450–5	10 ± 1	3.601	0.99
450–10	11 ± 1	3.600	0.96

$$m_{f_{\alpha'}} = m_{100\%\,\alpha'} * f_{\alpha'} + m_{100\%\gamma} * (1 - f_{\alpha'})$$

where $f_{\alpha'}$ is the fraction of martensite at room temperature and $m_{100\%\gamma}$ is the slope of the extrapolated curve for the 100 % austenite condition. $m_{f_{\alpha'}}$ is the slope of the interpolating curve at room temperature for the quenched sample and $m_{100\%\alpha'}$ is the unknown term in the equation. The initial austenite fraction is computed at 99 °C through the application of the lever rule between the 100 % γ extrapolated curve and the 100 % α′ reconstructed curve. Hence, the initial fraction of austenite was computed as 10 ± 1 %.

No other phase transformations were observed during the second quenching step or during the isothermal holding, meaning that a microstructure composed of martensite and austenite was observed at room temperature. The same procedure was used to estimate RA fractions in QP samples, considering the variation in A'C' segment due to expansion/contraction behavior during reheating and partitioning to avoid errors in the phase quantification, as described by Mola et al. [45]. In agreement with the results of the XRD analysis, the amount of RA calculated from the dilatometry data was 11 % and 10 % in the 450-5 and 250-10 sample, respectively.

Two conditions were selected for further analyses, namely 250-10 and 450-10. Such QP conditions were selected because they have same partitioning time. In addition, they feature the highest RA fraction among the QP samples at the selected temperatures.

The SEM images in Fig. 10 show the martensitic matrix present in the selected conditions. A slight difference in the tempering state of the QP

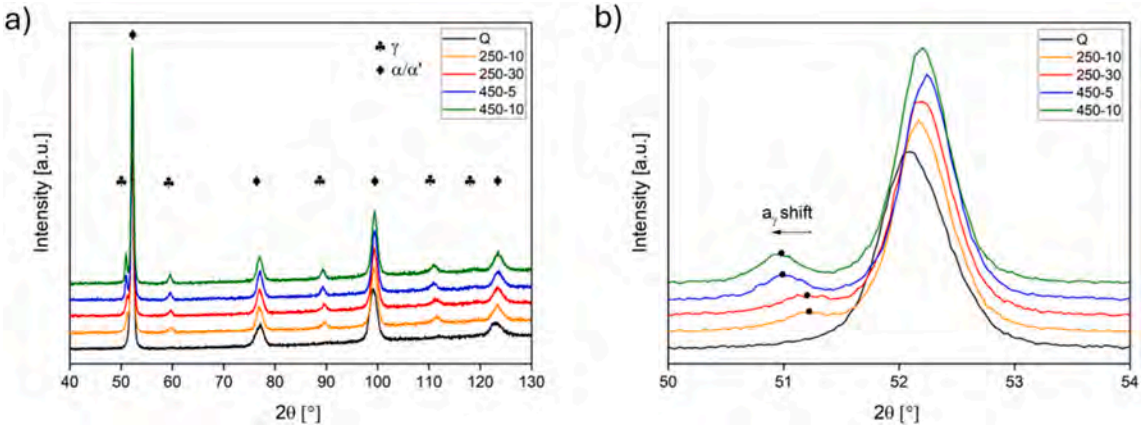

Fig. 8. XRD diffractograms of the a) heat-treated samples. b) Detail of the (111) austenite peak shift.

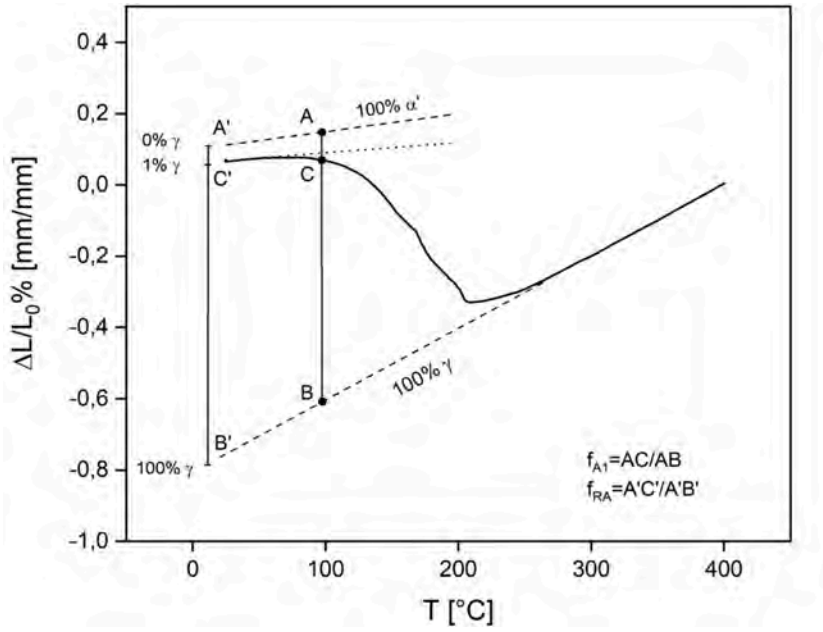

Fig. 9. Representative phase computation through dilatometry for Q sample. The change in the slope is magnified for visibility.

samples is observed, as an increased amount of transition carbides can be observed in 450–10 (Fig. 10c) compared to 250-10 (Fig. 10b) and especially with respect to the sample Q (Fig. 10a), where almost no carbide precipitation can be observed in the martensitic matrix [49]. A slight segregation appears to be present at the grain boundaries in all the different conditions, which was ascribed to the printing process. Although the identification of such submicrometric phases through SEM is not trivial, their elongated shape and their position at grain boundary suggests that these are chromium carbides $M_{23}C_6$, similar to those observed by Zhu et al. in PBF-LB AISI 420 samples [50].

EBSD phase maps of Fig. 11 show the presence of RA in the martensitic matrix of most samples, whose fraction differed from sample to sample. The Q specimen (Fig. 11b) though, presented only traces of RA. In QP samples, RA is homogeneously distributed within the microstructure, featuring either an elongated or a blocky morphology. Specimen 250-10 (Fig. 11e) presented a distribution of micro- and submicrometric RA grains. Specimen 450-10 (Fig. 11h) showed a higher fraction of RA, with coarser size. The fractions of RA measured by EBSD and those measured by XRD show some discrepancies, especially in the case of the 250-10 sample (≈2 % vs 8 %, respectively). Such differences

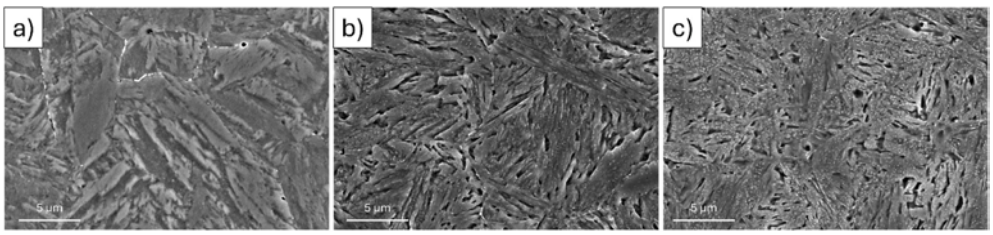

Fig. 10. SEM images of the microstructures of samples a) Q, b) 250-10, and c) 450-10.

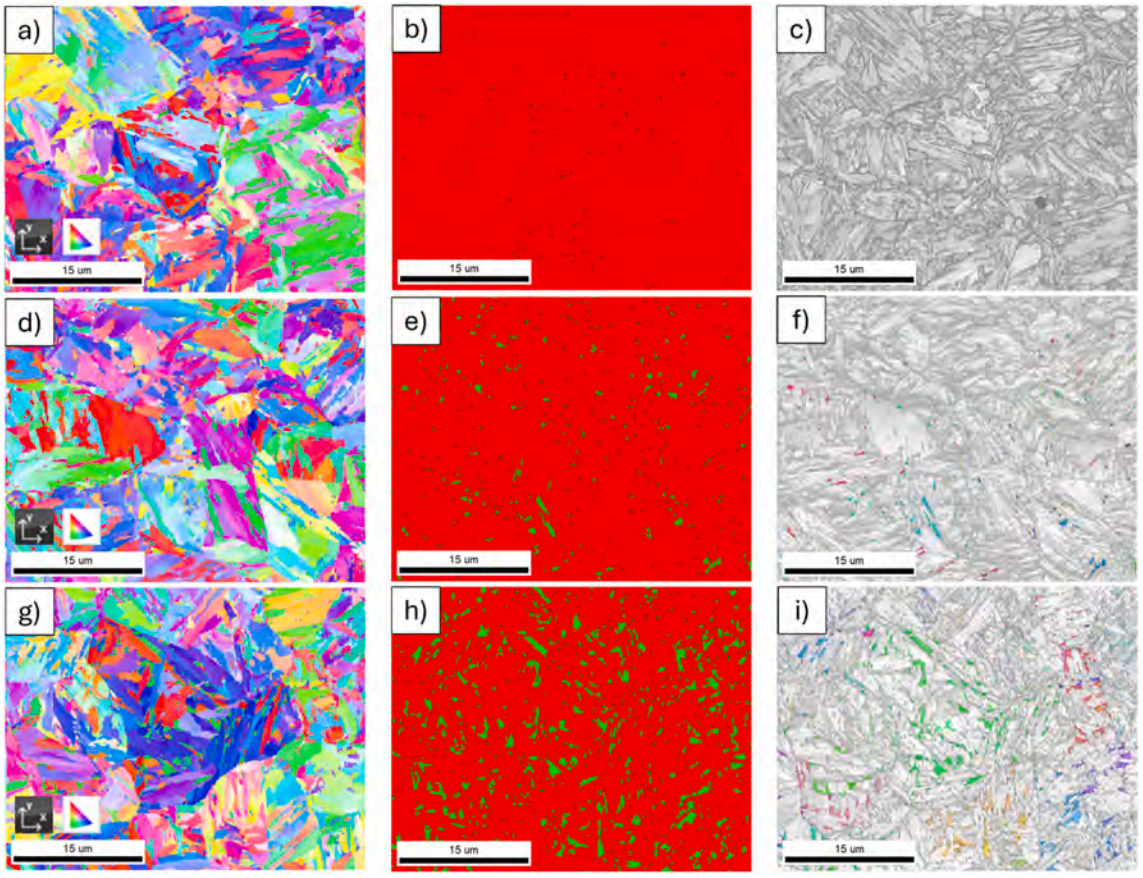

Fig. 11. EBSD maps for samples: a,b,c) Q, d,e,f) 250–10, g,h,i) 450-10. In particular, a), d), g) show the IPF; b), e), h) show the phase maps with retained austenite in green, martensite in red; and c), f), i) show the overlay of the RA subset IPF map and the band contrast map. (For interpretation of the references to colour in this figure legend, the reader is referred to the Web version of this article.)

could be attributed to the partial transformation of austenite into martensite during specimen preparation, to the small size of austenite grains that cannot be properly indexed with the selected set of measurement parameters, and to the limited size of the investigated area that could be not representative of the whole microstructure of the sample [30,51–53]. The analysis of the IPF maps overlapped with the band contrast maps (Fig. 11f–i) show colonies of untransformed austenite characterized by a similar orientation, belonging to the same PAG, which appear coarser than the ones observed in the AB condition reported in Fig. 5, due to the austenitization performed at 1100 °C.

3. Mechanical properties and fractography

The results of the microhardness $HV_{0.3}$ tests are presented in Fig. 12. The highest microhardness value was obtained with the Q sample (668 ± 11 $HV_{0.3}$), due to its non-tempered martensitic microstructure. Among the QP samples, the higher the partitioning temperature and time, the lower the microhardness: 250-10 sample shows the highest hardness value (538 ± 12 $HV_{0.3}$), whereas 450-10 sample shows the lowest one (502 ± 5 $HV_{0.3}$). Results of hardness tests are consistent with previous considerations about the different tempering stages obtained during QP treatments, as 250 °C treatments generally lead to higher hardness than 450 °C ones. Consistently, higher partitioning times lead to lower microhardness values. The standard deviation of the microhardness is small in the QP samples, showing that excellent microstructural homogeneity has been achieved in such samples due to the austenitization step of the heat treatment. On the contrary, the hardness of the AB sample features elevated standard deviation, that can be attributed to the less homogeneous microstructure resulting directly from the manufacturing process. The high solidification and cooling rates of the melt pool, steep thermal gradients, overlapping scanning tracks, and the intrinsic heat treatment during the PBF-LB, contributed to the development of such a complex microstructure, which is made of several constituents [29]. Despite the variability, the average hardness value of the AB sample is similar than those of the QP samples, meaning that the complex AB microstructure is mainly composed of tempered martensite (Fig. 5).

The tensile curves of the investigated conditions are presented in Fig. 13, while a summary of the main properties extracted from the curves are listed in Table 6. The QP specimens showed high mechanical properties, reaching a UTS of 1683 MPa in the 250-10 specimen. However, this sample also showed limited ductility (5 %) due to insufficiently-tempered – and hence brittle – martensite, a low fraction of RA, and likely fresh martensite. Also, the presence of detrimental transition carbides cannot be discarded. The 450-10 specimen features a lower UTS (1358 MPa) but the highest elongation value among studied samples (18 % at break), revealing adequate martensite tempering and carbon diffusion into RA. Specimen AB, even if characterized by a high fraction of RA, shows a combination of high UTS (1555 MPa) coupled with a low elongation (7 %). In this case, the presence of residual stresses induced by the thermal cycles associated with the AM process likely contributed to premature failure [54,55]. It has been reported that the high residual stresses of AB conditions are also responsible for a significant reduction in fatigue resistance [56] and fracture toughness [36]. Secondly, previous studies have shown that the intrinsic brittleness of the fine martensitic laths formed during PBF-LB processing can further reduce ductility [48].

The yield strengths of specimens 250-10 and 450-10 are 1058 MPa

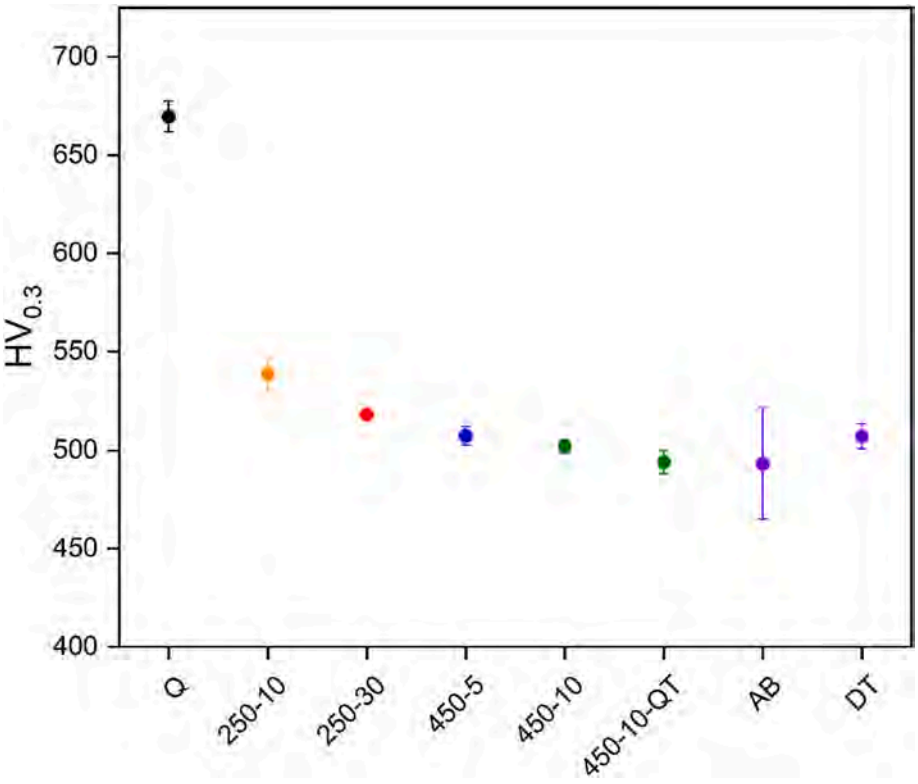

Fig. 12. Microhardness $HV_{0.3}$ values for the different heat-treated conditions.

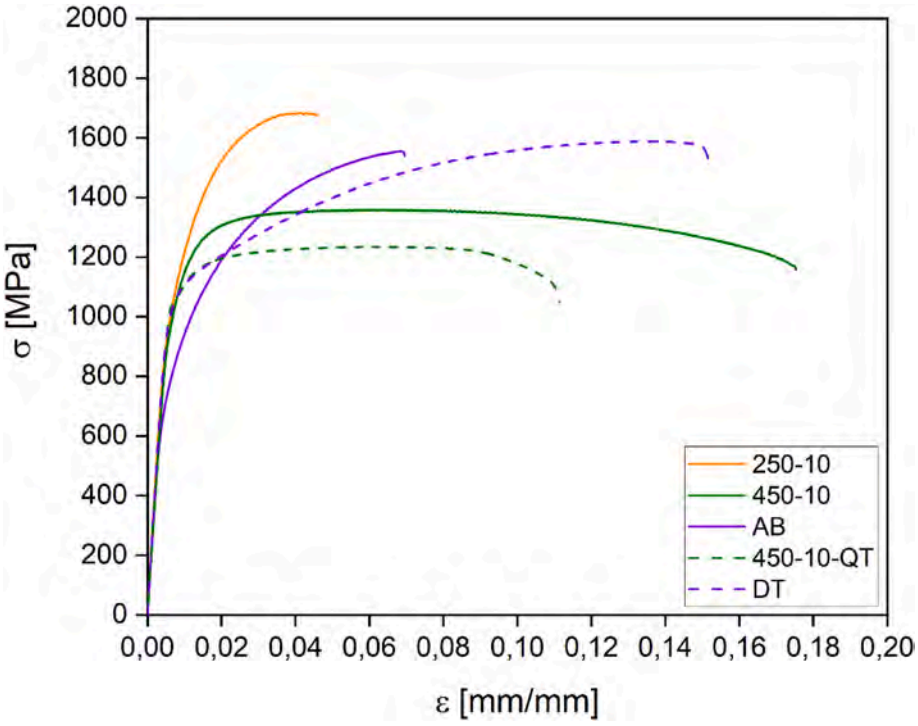

Fig. 13. Tensile stress-strain curves.

and 1040 MPa, respectively, while specimen AB shows a lower YS (765 MPa). This finding is consistent with the presence of a higher fraction of austenite in case AB, as shown by the results of EBSD (Fig. 11) and XRD analyses (Figs. 6 and 8). Indeed, the presence of the austenite has been previously reported to decrease the YS in multiphase TRIP-assisted steels proportionally to its volume fraction [57,58]. On the other hand, the DT sample shows high YS (1040 MPa) coupled with a high UTS (1589) and excellent elongation (15 %) as well. The tempering treatment decreased the specimen brittleness by means of adequate martensite tempering and reduction of the residual stresses, leading to an excellent

Table 6
Tensile properties of the tested specimens.

Sample	YS [MPa]	UTS [MPa]	A%
250–10	1058	1683	5
450–10	1040	1358	18
AB	765	1555	7
450-10-QT	1054	1235	11
DT	1040	1589	15

combination of tensile strength and ductility. Furthermore, inheriting the fine-grained microstructure from the PBF-LB process, the DT sample retained a high level of dislocation and grain boundary strengthening [48], contributing to its favorable combination of strength and ductility. However, it is worth mentioning that previous studies have shown that DT can leave a certain degree of residual stress, which negatively affects the fatigue resistance and fracture toughness of steels [59].

Lastly, the tensile curve of the comparative 450-10-QT specimen is also presented in Fig. 13. This specimen was aimed at sharing the same level of martensite tempering as the equivalent QP specimen. Such condition has been used already in previous studies for comparison and is considered as a benchmark condition [20,31,46]. However, the 450-10-QT specimen presented lower UTS and elongation in comparison to the 450-10 specimen. Nevertheless, it is important to note that all the tested samples have a low thickness (3 mm). As a result, any defects in the specimens may lead to variability in the mechanical performance due to the small cross-sectional area, with elongation at break and UTS being particularly affected. Given the thin wall structure of the specimens used in this material characterization, the results can be considered as a lower boundary for the material's performance.

Instantaneous strain-hardening coefficients n are reported in Fig. 14. The initial value of the hardening coefficient n is correlated with martensite tempering, as observed by Findley et al. [46] in previous studies, but its evolution during the deformation process is correlated with microstructural features such as retained austenite content and stability, grain size, morphology and orientation. Consistently with that, the 250-10 sample showed higher n than the 450-10 sample up to ε_{true} values of 0.04, where breakage occurred due to its microstructure composed of low-tempered martensite and low-stability RA. The 450-10 instead, featured a slower decrease in n at higher strains thanks to the presence of stable RA at higher deformation stages, delaying necking to higher strains. In comparison to the 450-10-QT sample, the QP equivalent one showed higher initial n because of the RA presence and transformation even at low strains. This behavior was observed in previous studies on QP-treated AISI 4140 steels, independent of RA amount [19]. AB sample shows a smooth decrease thanks to the high amount of RA and its strain-induced transformation. However, the brittleness of the martensitic matrix in this condition does not allow a high ductility, and the failure of the specimen occurs prematurely. This consideration is supported by the DT sample, which shows instead the presence of an intense TRIP effect at medium strains which delays the onset of necking to the highest value between all the samples and leading to the highest uniform elongation observed. The high carbon concentration in austenite in the DT sample (1.02 wt%) is close to the one of the AB sample (1.07 wt%), however the differences in the work-hardening behavior can be ascribed to the surrounding microstructure, which has been repeatedly observed to play a crucial role in exploiting the effect of strain-induced transformation of RA, leading to different sets of final properties [48,60].

The fracture surfaces of tensile samples AB, 250-10 and 450-10 are presented in Fig. 15. The fracture surfaces of specimen AB (Fig. 15a) are mainly characterized by brittle features and very small dimples. Specimen 250-10 (Fig. 15b) shows a more variable behavior, featuring wider ductile areas alternated with more brittle regions. It can be inferred that the low martensite tempering accompanied by austenite with low carbon content is not able to provide sufficient ductility to the material. In contrast, the 450-10 specimen shows a microscopically ductile fracture surface, as evidenced by the widespread presence of coarser dimples within the fracture surface. The high properties of the 450-10 sample are ascribed to the presence of properly tempered martensite and enough stable austenite, as inferred by its high carbon content (0.96 %). Nevertheless, typical PBF-LB defects, such as lack-of-fusion and pores (as visible in Fig. 15c), were observed in all the analyzed surfaces. It should

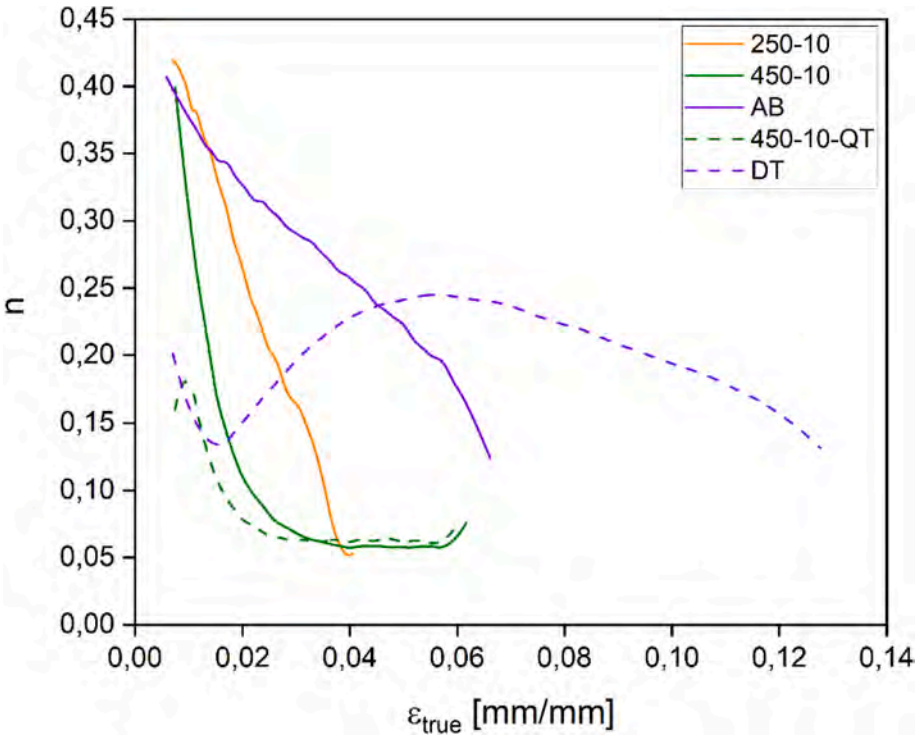

Fig. 14. Work hardening coefficients n.

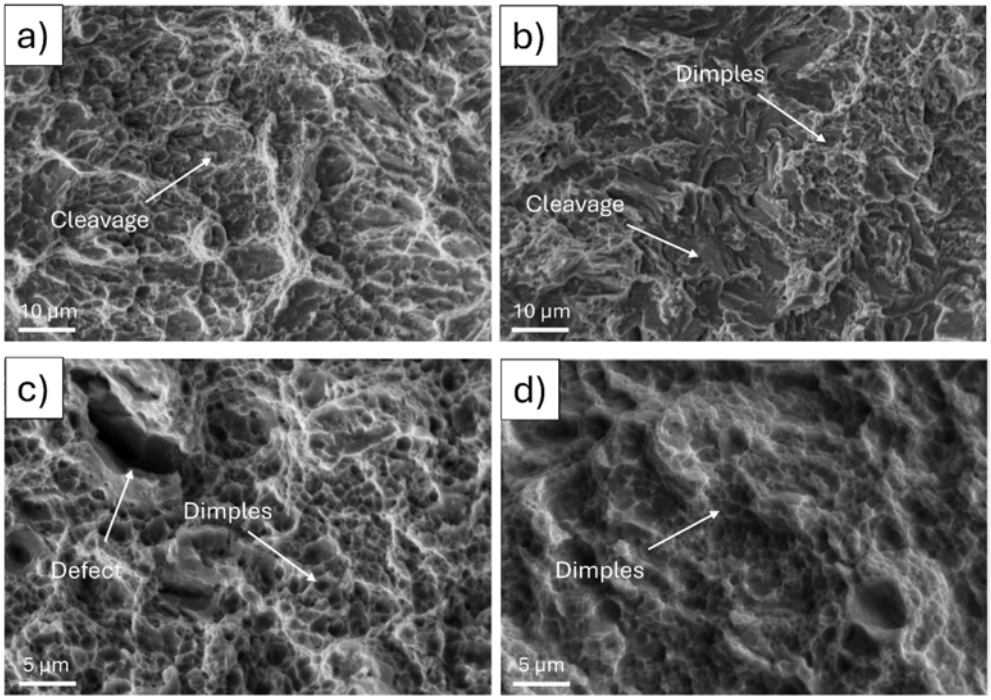

Fig. 15. Fracture surfaces. a) AB, b) 250-10, c) 450–10, d) DT.

be emphasized that the presence of these defects tends to lower mechanical strength and ductility, and they are preferential sites for crack nucleation. In fact, brittle regions are usually found in the proximity of these defects. After comparing the fracture surfaces of AB and 450-10 specimens, both of which are characterized by substantial amounts of retained austenite, it can be concluded that the presence of retained austenite by itself does not guarantee a significant improvement of ductility in the material, and the state of the matrix should be controlled for an optimized final performance.

4. Conclusions

In this work, fully dense AISI 420 specimens were successfully produced via PBF-LB, without the presence of cracks or major defects. The AB material exhibited a fine martensitic matrix with a significant fraction of RA (16 %), which contributed to a high UTS of 1555 MPa. However, despite the high strength, the elongation is low (7 %). Different heat-treatment strategies have been explored to achieve a combination of high strength and improved ductility in PBF-LB manufactured AISI 420 steel, namely quenching and partitioning and direct tempering. The results demonstrate that different processing routes can be effectively used to tailor the microstructure and the final mechanical properties in the selected material. QP and tempering treatments offer alternative strategies to optimize strength-ductility trade-offs.

Different time and temperature combinations for QP treatments were explored. The most promising treatment was found to be 450 °C for 10 min, which resulted in an optimal combination of UTS (1358 MPa) and elongation (18 %). Microstructural analyses revealed the presence of a tempered martensitic matrix in this condition. This matrix was coarser than the as-built material, a result of the high-temperature austenitization performed at 1100 °C. Moreover, the RA fraction (11 %) was distributed throughout the microstructure, appearing in both elongated and blocky morphologies. In addition to the effect of microstructural coarsening and the more uniform RA distribution, the reduction of residual stresses likely played a role in enhancing ductility. The improved ductility compared to the comparative quenched and tempered condition (450-10-QT) is mainly attributed to the presence of stable RA and its controlled transformation during deformation, which is more effective in delaying necking for higher strains improving ductility and especially uniform elongation. The sample partitioned at 250 °C for 10 min instead, featuring lower martensite tempering and lower austenite stability, shows limited ductility (5 %) even in presence of a consistent fraction of retained austenite (8 %). The achievement of both stable retained austenite and sufficiently tempered martensite appears crucial for optimizing final mechanical response in QP-treated conditions.

Among the conditions investigated, DT and AB exhibited a similar RA fraction, and DT displayed significantly higher tensile properties and improved ductility, which are primarily attributed to the fine martensitic microstructure and the reduction of residual stresses. The DT condition also featured improved work-hardening behavior, as it exhibited an intense TRIP effect at medium strains, delaying necking and leading to the highest uniform elongation among all conditions tested.

The results indicate that both quenching and partitioning, and direct tempering are promising routes for improving the ductility of PBF-LB AISI 420 steel while maintaining high strength. However, the choice of the optimal heat treatment depends on the specific application. The different microstructures obtained through QP and DT could have a significant impact not only on tensile properties but also on other properties such as fatigue resistance and fracture toughness. Moreover, QP and especially DT can be considered a viable energy-saving strategy, to the low temperatures and times involved compared to conventional quenching and tempering strategies. DT is particularly less energy demanding. Future studies should therefore focus on investigating the fatigue behavior and fracture toughness of these materials to better understand their suitability for specific applications.

CRediT authorship contribution statement

M. Belfi: Writing – original draft, Methodology, Investigation, Conceptualization. **G. Lupi:** Writing – original draft, Methodology, Investigation, Conceptualization. **P. Martin:** Writing – review & editing, Methodology, Investigation. **M. Santofimia:** Writing – review & editing, Supervision, Resources, Methodology, Conceptualization. **A. Gruttadauria:** Writing – review & editing, Supervision. **R. Casati:** Writing – review & editing, Supervision, Resources. **S. Barella:** Writing – review & editing, Supervision, Resources.

Declaration of competing interest

The authors declare that they have no known competing financial interests or personal relationships that could have appeared to influence the work reported in this paper.

Acknowledgments

The authors thank Mimete s.r.l and Andrea Tarabiono for the support provided for the experimental activity. The authors acknowledge the Department of Materials Science and Engineering of TU Delft, especially to C. Kwakernaak, R. Huizenga and N. Geelhofs for their technical support. Thanks to M. Ishola and L. Rovatti from the Mechanical Engineering department at Politecnico di Milano.

Data availability

Data will be made available on request.

References

[1] C. Lesch, N. Kwiaton, F.B. Klose, Advanced High Strength Steels (AHSS) for automotive applications – tailored properties by smart microstructural adjustments, Steel Res. Int. 88 (10) (2017) 1–21, https://doi.org/10.1002/srin.201700210.
[2] O. Bouaziz, H. Zurob, M. Huang, Driving force and logic of development of advanced high strength steels for automotive applications, Steel Res. Int. 84 (10) (2013) 937–947, https://doi.org/10.1002/srin.201200288.
[3] J. Speer, D.K. Matlock, B.C. De Cooman, J.G. Schroth, Carbon partitioning into austenite after martensite transformation, Acta Mater. 51 (9) (2003) 2611–2622, https://doi.org/10.1016/S1359-6454(03)00059-4.
[4] A.J. Clarke, et al., Carbon partitioning to austenite from martensite or bainite during the quench and partition (Q&P) process: a critical assessment, Acta Mater. 56 (1) (2008) 16–22, https://doi.org/10.1016/j.actamat.2007.08.051.
[5] D. De Knijf, R. Petrov, C. Föjer, L.A.I. Kestens, Effect of fresh martensite on the stability of retained austenite in quenching and partitioning steel, Mater. Sci. Eng. 615 (2014) 107–115, https://doi.org/10.1016/j.msea.2014.07.054.
[6] J. Mola, B.C. De Cooman, Quenching and partitioning (Q&P) processing of martensitic stainless steels, Metall Mater Trans A Phys Metall Mater Sci 44 (2) (2013) 946–967, https://doi.org/10.1007/s11661-012-1420-1.
[7] C. Celada-Casero, C. Kwakernaak, J. Sietsma, M.J. Santofimia, The influence of the austenite grain size on the microstructural development during quenching and partitioning processing of a low-carbon steel, Mater. Des. 178 (2019) 107847, https://doi.org/10.1016/j.matdes.2019.107847.
[8] S. Kaar, D. Krizan, R. Schneider, C. Sommitsch, Impact of Si and Al on Microstructural Evolution and Mechanical Properties of Lean Medium Manganese Quenching and Partitioning Steels, Steel Res. Int. 91 (10) (2020), https://doi.org/10.1002/srin.202000181.
[9] E. De Moor, J.G. Speer, D.K. Matlock, D.N. Hanlon, Effect of retained austenite on tensile behavior of AHSS revisited, Materials Science and Technology Conference and Exhibition 2011, MS and T'11 1 (October 2015) 568–579, 2011.
[10] E. de Moor, S. Lacroix, A.J. Clarke, J. Penning, J.G. Speer, Effect of retained austenite stabilized via quench and partitioning on the strain hardening of martensitic steels, Metall Mater Trans A Phys Metall Mater Sci 39 (11) (2008) 2586–2595, https://doi.org/10.1007/s11661-008-9609-z.
[11] M. Soleimani, A. Kalhor, H. Mirzadeh, Transformation-induced plasticity (TRIP) in advanced steels: a review, Mater. Sci. Eng. 795 (July) (2020), https://doi.org/10.1016/j.msea.2020.140023.
[12] S. Ebner, R. Schnitzer, E. Maawad, C. Suppan, C. Hofer, Influence of partitioning parameters on the mechanical stability of austenite in a Q&P steel: a comparative in-situ study, Materialia 15 (February) (2021) 101033, https://doi.org/10.1016/j.mtla.2021.101033.
[13] D. De Knijf, C. Föjer, L.A.I. Kestens, R. Petrov, Factors influencing the austenite stability during tensile testing of Quenching and Partitioning steel determined via in-situ Electron Backscatter Diffraction, Mater. Sci. Eng. 638 (2015) 219–227, https://doi.org/10.1016/j.msea.2015.04.075.
[14] I. Miettunen, S. Ghosh, M.C. Somani, S. Pallaspuro, J. Kömi, Competitive mechanisms occurring during quenching and partitioning of three silicon variants of 0.4 wt.% carbon steels, J. Mater. Res. Technol. 11 (2021) 1045–1060, https://doi.org/10.1016/j.jmrt.2021.01.085.
[15] B. Kim, J. Sietsma, M.J. Santofimia, The role of silicon in carbon partitioning processes in martensite/austenite microstructures, Mater. Des. 127 (April) (2017) 336–345, https://doi.org/10.1016/j.matdes.2017.04.080.
[16] C.B. Finfrock, et al., Elucidating the temperature dependence of TRIP in Q&P steels using synchrotron X-Ray diffraction, constituent phase properties, and strain-based kinetics models, Acta Mater. 237 (2022), https://doi.org/10.1016/j.actamat.2022.118126.
[17] X. Han, Y. Zhong, P. Xin, Z. Cui, J. Chen, Research on one-step quenching and partitioning treatment and its application in hot stamping process, Proc Inst Mech Eng B J Eng Manuf 231 (11) (2017) 1972–1982, https://doi.org/10.1177/0954405415616062.
[18] H. Kong, et al., One-step quenching and partitioning treatment of a commercial low silicon boron steel, Mater. Sci. Eng. 707 (July) (2017) 538–547, https://doi.org/10.1016/j.msea.2017.09.038.
[19] M. Belfi, et al., On the strain hardening and tensile properties of AISI 4140 steel via single-step quenching and partitioning treatments, Steel Res. Int. 2400513 (2024) 2400513, https://doi.org/10.1002/srin.202400513.
[20] S. Barella, M. Belfi, A. Gruttadauria, C. Liu, Y. Peng, Metallurgical and mechanical investigation on single-step quenching and partitioning thermal treatments on commercial low alloyed 30MnV6 steel, Metall Mater Trans A Phys Metall Mater Sci 55 (2023) 513–522, https://doi.org/10.1007/s11661-023-07262-y.
[21] S. Barella, et al., The reliability of single-step and double-step quench and partitioning heat treatments on an AISI 420A low carbon martensitic stainless steel, Metall Mater Trans A Phys Metall Mater Sci 54 (10) (2023) 3957–3972, https://doi.org/10.1007/s11661-023-07145-2.
[22] S.D. Nath, H. Irrinki, G. Gupta, M. Kearns, O. Gulsoy, S. Atre, Microstructure-property relationships of 420 stainless steel fabricated by laser-powder bed fusion, Powder Technol. 343 (2019) 738–746, https://doi.org/10.1016/j.powtec.2018.11.075.
[23] K. Saeidi, et al., Ultra-high strength martensitic 420 stainless steel with high ductility, Addit. Manuf. 29 (July) (2019) 100803, https://doi.org/10.1016/j.addma.2019.100803.
[24] M.M. Francois, et al., Modeling of additive manufacturing processes for metals: challenges and opportunities, Curr. Opin. Solid State Mater. Sci. 21 (4) (2017) 198–206, https://doi.org/10.1016/j.cossms.2016.12.001.
[25] S.S. Babu, L. Love, R. Dehoff, W. Peter, T.R. Watkins, S. Pannala, Additive manufacturing of materials: opportunities and challenges, MRS Bull. 40 (12) (2015) 1154–1161, https://doi.org/10.1557/mrs.2015.234.
[26] E.H. Sabuz, I. Shabib, Microstructure, Hardness, and Tensile Properties of Additively Manufactured Low-Alloy Steel: Rev. (2025) 2400421, https://doi.org/10.1002/srin.202400421.
[27] P. Krakhmalev, I. Yadroitsava, G. Fredriksson, I. Yadroitsev, In situ heat treatment in selective laser melted martensitic AISI 420 stainless steels, Mater. Des. 87 (2015) 380–385, https://doi.org/10.1016/j.matdes.2015.08.045.
[28] S.D. Nath, et al., Effects of Nb and Mo on the microstructure and properties of 420 stainless steel processed by laser-powder bed fusion, Addit. Manuf. 28 (February) (2019) 682–691, https://doi.org/10.1016/j.addma.2019.06.016.
[29] K. Saeidi, et al., Ultra-high strength martensitic 420 stainless steel with high ductility, Addit. Manuf. 29 (March) (2019) 100803, https://doi.org/10.1016/j.addma.2019.100803.
[30] A. Sierra-Soraluce, et al., Effect of microstructure on tensile properties of quenched and partitioned martensitic stainless steels, Mater. Sci. Eng. 864 (2023) 144540, https://doi.org/10.1016/j.msea.2022.144540. December 2022.
[31] S. Barella, M. Belfi, A. Gruttadauria, P. Cetto, C. Liu, Y. Peng, Influence of quenching and partitioning on the mechanical properties of low-silicon 33MnCrB5 boron steel, Steel Res. Int. (2023) 2300622, https://doi.org/10.1002/srin.202300622.
[32] L. Lutterotti, Maud: a Rietveld analysis program designed for the internet and experiment integration, Acta Crystallogr. A 56 (s1) (Aug. 2000), https://doi.org/10.1107/s0108767300021954 s54–s54.
[33] N.H. Van Dijk, et al., Thermal stability of retained austenite in TRIP steels studied by synchrotron X-ray diffraction during cooling, Acta Mater. 53 (20) (2005) 5439–5447, https://doi.org/10.1016/j.actamat.2005.08.017.
[34] B. Denand, et al., Carbon content evolution in austenite during austenitization studied by in situ synchrotron X-ray diffraction of a hypoeutectoid steel, Materialia 10 (January) (2020), https://doi.org/10.1016/j.mtla.2020.100664.
[35] X. Zhao, et al., Fabrication and characterization of AISI 420 stainless steel using selective laser melting, Mater. Manuf. Process. 30 (11) (2015) 1283–1289, https://doi.org/10.1080/10426914.2015.1026351.
[36] G. Lupi, G. Minerva, L. Patriarca, R. Casati, S. Beretta, Fracture toughness of AlSi10Mg alloy produced by LPBF: effects of orientation and heat treatment, Int. J. Fract. 247 (3) (2024) 329–344, https://doi.org/10.1007/s10704-024-00787-2.
[37] J. Hidalgo, K.O. Findley, M.J. Santofimia, Thermal and mechanical stability of retained austenite surrounded by martensite with different degrees of tempering, Mater. Sci. Eng. 690 (2017) 337–347, https://doi.org/10.1016/j.msea.2017.03.017.
[38] L. Wu, et al., Microstructure and mechanical characterization of additively manufactured Fe11Cr8Ni5Co3Mo martensitic stainless steel, Mater. Char. 203 (March) (2023) 113106, https://doi.org/10.1016/j.matchar.2023.113106.
[39] F.S.H.B. Freeman, J. Sharp, J. Xi, I. Todd, Influence of solidification cell structure on the martensitic transformation in additively manufactured steels, Addit. Manuf. 30 (October) (2019) 100917, https://doi.org/10.1016/j.addma.2019.100917.
[40] J. Akram, P. Chalavadi, D. Pal, B. Stucker, Understanding grain evolution in additive manufacturing through modeling, Addit. Manuf. 21 (May 2018) 255–268, https://doi.org/10.1016/J.ADDMA.2018.03.021.
[41] K. Hagihara, T. Nakano, Control of Anisotropic Crystallographic texture in powder bed fusion additive manufacturing of metals and Ceramics—A review, J. Occup. Med. 74 (4) (Nov. 2021) 1760–1773, https://doi.org/10.1007/S11837-021-04966-7, 2021 74:4.
[42] G. Lupi, E. Bettini, F. Deirmina, R. Casati, Microstructural and mechanical properties of a novel cobalt and titanium free maraging steel for laser powder bed fusion, J. Mater. Res. Technol. 30 (May 2024) 1269–1278, https://doi.org/10.1016/J.JMRT.2024.03.088.
[43] H. Nakagawa, T. Miyazaki, Effect of retained austenite on the microstructure and mechanical properties of martensitic precipitation hardening stainless steel,

J. Mater. Sci. 34 (16) (1999) 3901–3908, https://doi.org/10.1023/A:1004626907367.
[44] L. Heemann, et al., Adjustment of mechanical properties of medium manganese steel produced by laser powder bed fusion with a subsequent heat treatment, Materials 14 (11) (2021), https://doi.org/10.3390/ma14113081.
[45] S. Kumar, S.B. Singh, Quenching and partitioning (Q&P) steel: alloy design, phase transformation and evolution of microstructure, Metall Mater Trans A Phys Metall Mater Sci 54 (8) (2023) 3134–3156, https://doi.org/10.1007/s11661-023-07085-x.
[46] K.O. Findley, J. Hidalgo, R.M. Huizenga, M.J. Santofimia, Controlling the work hardening of martensite to increase the strength/ductility balance in quenched and partitioned steels, Mater. Des. 117 (2017) 248–256, https://doi.org/10.1016/j.matdes.2016.12.065.
[47] S.M.C. Van Bohemen, The nonlinear lattice expansion of iron alloys in the range 100-1600 K, Scr. Mater. 69 (4) (2013) 315–318, https://doi.org/10.1016/j.scriptamat.2013.05.009.
[48] M. Thrun, V. Euser, A. Clarke, K. Clarke, Tuning austenite stability through prior microstructure control in a low-alloy Q&P steel, Materialia 38 (September) (2024) 102261, https://doi.org/10.1016/j.mtla.2024.102261.
[49] Y. Tian, K. Chadha, C. Aranas, Laser powder bed fusion of ultra-high-strength 420 stainless steel: microstructure characterization, texture evolution and mechanical properties, Mater. Sci. Eng. 805 (January) (2021) 140790, https://doi.org/10.1016/j.msea.2021.140790.
[50] H. Zhu, Y. Li, B. Li, Z. Zhang, C. Qiu, Effects of low-temperature tempering on microstructure and properties of the laser-cladded AISI 420 martensitic stainless steel coating, Coatings 8 (12) (2018), https://doi.org/10.3390/COATINGS8120451.
[51] L.A. Pinto, D. Pérez Escobar, O.S.H. Santos, N.I.A. Lopes, J.R.G. Carneiro, R. Ribeiro-Andrade, Influence of surface preparation method on retained austenite quantification, Mater. Today Commun. 24 (February) (2020) 101226, https://doi.org/10.1016/j.mtcomm.2020.101226.
[52] A. Mostafapour, A. Ebrahimpour, T. Saied, Identification of retained Austenite, ferrite, bainite and martensite in the microstructure of TRIP steel, International Journal of Iron & Steel Society of Iran 13 (2) (2016) 1–6.
[53] M. Carpio, J. Calvo, O. García, J.P. Pedraza, J.M. Cabrera, Heat treatment design for a qp steel: effect of partitioning temperature, Metals 11 (7) (2021) 1–15, https://doi.org/10.3390/met11071136.
[54] I. Serrano-Munoz, et al., Scanning manufacturing parameters determining the residual stress State in LPBF IN718 small parts, Adv. Eng. Mater. 23 (7) (2021), https://doi.org/10.1002/adem.202100158.
[55] K. Kempen, B. Vrancken, S. Buls, L. Thijs, J. Van Humbeeck, J.P. Kruth, Selective Laser melting of crack-free high density M2 high speed steel parts by baseplate preheating, Journal of Manufacturing Science and Engineering, Transactions of the ASME 136 (6) (2014) 1–7, https://doi.org/10.1115/1.4028513.
[56] S. Cao, H. Zhang, J. Hu, C. Li, B. Li, Fatigue life prediction model for shot-peened laser powder bed fused 304L steel considering residual stress relaxation and defect distribution, Eng. Fail. Anal. 162 (May) (2024) 108423, https://doi.org/10.1016/j.engfailanal.2024.108423.
[57] P.J. Jacques, Q. Furnémont, F. Lani, T. Pardoen, F. Delannay, Multiscale mechanics of TRIP-assisted multiphase steels: I. Characterization and mechanical testing, Acta Mater. 55 (11) (2007) 3681–3693, https://doi.org/10.1016/j.actamat.2007.02.029.
[58] A.P. Pierman, O. Bouaziz, T. Pardoen, P.J. Jacques, L. Brassart, The influence of microstructure and composition on the plastic behaviour of dual-phase steels, Acta Mater. 73 (2014) 298–311, https://doi.org/10.1016/j.actamat.2014.04.015.
[59] F. Deirmina, P.A. Davies, R. Casati, Effects of powder Atomization route and post-processing thermal treatments on the mechanical properties and fatigue resistance of additively manufactured 18Ni300 maraging steel, Adv. Eng. Mater. 24 (4) (2022), https://doi.org/10.1002/adem.202101011.
[60] J. Chiang, B. Lawrence, J.D. Boyd, A.K. Pilkey, Effect of microstructure on retained austenite stability and work hardening of TRIP steels, Mater. Sci. Eng. 528 (13–14) (2011) 4516–4521, https://doi.org/10.1016/j.msea.2011.02.032.